npj | quantum materials

Article

Published in partnership with Nanjing University

https://doi.org/10.1038/s41535-025-00807-x

Distinct terahertz nonlinear and Raman responses in cuprate superconductors $Bi_2Sr_2CaCu_2O_{8+x}$

Kota Katsumi[1] ✉, Yann Gallais[2] ✉ & Ryo Shimano[3,4] ✉

Nonlinear light-matter interaction at low energy, particularly in the terahertz (THz) frequency range, hosts unique phenomena distinct from the optical excitation with photon energy of a few eV. In cuprate superconductors $Bi_2Sr_2CaCu_2O_{8+x}$, the THz nonlinear response is identified via the optical reflectivity change and interpreted as the amplitude mode of the superconducting condensate, namely the Higgs mode [K. Katsumi et al., *Phys. Rev. Lett.* 120, 117001 (2018)]. However, the origin of the THz nonlinearity has been questioned because the pair-breaking process, identified in Raman spectroscopy, can also contribute to it. Here, we reexamined the THz-driven nonequilibrium dynamics in cuprates $Bi_2Sr_2CaCu_2O_{8+x}$ by comparing it with the Raman susceptibility. In the optical reflectivity change, we found an oscillatory behavior following the squared THz waveform (THz Kerr signal), as well as the relaxation of the quasiparticle excitation. Careful insight into the data revealed that the oscillatory and decaying contributions exhibit different doping dependence. Remarkably, the doping and temperature evolutions of the THz Kerr signal are distinct from those of the Raman susceptibility, which is described by the pair-breaking due to diamagnetic light–matter interaction. These results indicate the importance of the paramagnetic light–matter coupling in the THz Kerr signal in the cuprate superconductors, likely arising from the Higgs mode.

Light–matter interaction in quantum materials is one of the key aspects to elucidate their properties. In particular, terahertz (THz) frequency range is of great interest as it enables access to rich low-energy excitations in such materials as a consequence of the complex interplay between charge, spin, orbital, and lattice. For instance, in the case of the linear response in dirty-limit BCS superconductors, the real part of the THz optical conductivity shows a reduction in its spectral weight below twice the superconducting (SC) gap 2Δ, which is transferred to the zero-frequency delta-function[1].

Recent advances in generating an intense THz pulse give access to the nonlinear light–matter interaction, which can provide information unreachable by linear light–matter coupling[2,3]. In BCS superconductors, THz nonlinear responses, investigated by pump-probe spectroscopy or third-harmonic generation (THG), were initially ascribed to the amplitude mode of the SC order parameter, referred to as the Higgs mode[4–8]. This illustrates the unique information obtained by the nonlinear optical spectroscopy, which cannot be accessed by the linear response[8]. Furthermore, it opens a new avenue toward coherent light control of SC order parameters. However, subsequent theoretical works showed that the THz nonlinear response of a clean BCS superconductor, where only diamagnetic light–matter coupling terms contribute, is actually governed by charge density fluctuations (CDF). The CDF contribution leads to a pair-breaking peak at twice the SC gap and is usually thought to be the dominant contribution to the Raman response, whose BCS non-resonant diamagnetic terms are essentially identical to the THz third-order nonlinear response[9]. Later, the importance of the paramagnetic light–matter coupling terms in boosting the Higgs contribution to the THz nonlinear response was pointed out in the presence of finite disorder, indicating that the relative hierarchy of the two contributions depends on the disorder level[10–17]. In the specific case of a dirty-limit superconductor like NbN with a relatively high disorder level, the nonlinear response was argued to be dominated by the Higgs mode[13]. Yet, experimentally disentangling the diamagnetic and paramagnetic contributions to the THz nonlinear signal is challenging as both display the same resonant enhancement when the twice the THz pump frequency matches 2Δ[10–17].

More recently, THz two-dimensional coherent spectroscopy (THz 2DCS) was introduced to single out the nonlinear paramagnetic light–matter

[1]Center for Quantum Phenomena, Department of Physics, New York University, New York, NY, USA. [2]Université Paris Cité, Matériaux et Phénoménes Quantiques UMR CNRS 7162, Paris, France. [3]Department of Physics, The University of Tokyo, Hongo, Tokyo, Japan. [4]Cryogenic Research Center, The University of Tokyo, Yayoi, Tokyo, Japan. ✉e-mail: kota.katsumi@nyu.edu; yann.gallais@u-paris.fr; shimano@phys.s.u-tokyo.ac.jp

coupling of the Higgs mode in NbN[18]. This also demonstrated that the excitation process in THz nonlinear response can be essentially different from that of the Raman response, which is performed in the optical frequency range of a few eV and is usually assigned to the CDF contribution[9,19].

Having gained a deeper understanding of the Higgs mode in conventional superconductors, studies have been expanded to unconventional superconductors. In the case of cuprate superconductors, the observation of the Higgs mode can provide unique insight into their SC properties, including the SC fluctuations[20], the interplay between SC and competing orders[21], and the coupling of the SC order parameter to lattice or spin excitations. However, the distinction between the Higgs mode and CDF is less clear-cut in the case of cuprate superconductors, which are usually in the clean limit and the diamagnetic terms are therefore expected to play a leading role in the THz nonlinearity[14,15]. Therefore, although the THz nonlinearity in cuprates has been reported by several experiments and interpreted as the Higgs mode[20–24], its origin is still under discussion[14,15,25–27].

To investigate the nature of the THz nonlinearity in cuprate superconductors, we revisited our THz pump-optical probe (TPOP) spectroscopy in cuprate superconductors $Bi_2Sr_2CaCu_2O_{8+x}$ (Bi2212), in ref. 22 by comparing it with Raman experiments performed on the same single crystals. In the SC state, we identified the relaxation of the quasiparticle (QP) excitation (decaying signal), as well as the forced oscillation following the squared THz waveform, i.e., the THz Kerr signal, where the refractive index at the probing wavelength at 800 nm is modulated by the THz pump[28]. Remarkably, the THz Kerr signal displays a markedly different doping dependence from the Raman susceptibility.

We further compare the temperature dependence of the THz Kerr signal with that of the extracted real part of the Raman susceptibility evaluated at the THz pump frequency of 0.7 THz. The extracted Raman susceptibility does not exhibit an increase below the SC transition temperature T_c, in stark contrast to that of the THz Kerr signal, which displays a sharp increase below T_c. These findings lead us to conclude that the THz Kerr and Raman responses in the SC state arise from different light–matter coupling terms: the Raman response is dominated by the CDF contribution from the diamagnetic terms, while the THz Kerr response arises from a different origin.

Results

THz-Kerr signals

A schematic of TPOP spectroscopy is illustrated in Fig. 1a. We measured the THz pump-induced transient reflectivity change at 800 nm (1.55 eV in photon energy), varying the delay time between the pump and the probe pulses (t_{pp}). In Fig. 1b, we present the waveform of the THz pulse (left) and its power spectrum (right), centered at 0.7 THz. The polarization of the THz electric field is along the Cu–O bond of the sample, and that of the probe is parallel or perpendicular to the pump. In the case of Bi2212, whose symmetry belongs to the D_{4h} point group, we obtain the polarization-independent A_{1g} component of the reflectivity change $\Delta R/R$ by adding $\Delta R/R$ for the probe parallel or perpendicular to the pump[22]. Similarly, the B_{1g} component is obtained by subtracting $\Delta R/R$ for the probe perpendicular to the pump from that for the probe parallel to the pump. We performed TPOP experiments on the Bi2212 families as summarized in Table 1.

Figure 1c presents the A_{1g} and B_{1g} parts of the THz pump-induced reflectivity change $\Delta R/R$ for the selected Bi2212 samples in the SC state at 10 K, adapted from ref. 22. In all the Bi2212 samples, both A_{1g} and B_{1g} parts of $\Delta R/R$ display an oscillatory behavior following the two peaks in the THz-pump time trace indicated by the black vertical dashed lines. As reported in ref. 22, the intensity of the oscillatory signal follows the squared THz electric field (E-field), and the third-order nonlinear process is called the THz Kerr signal[28]. One can also find the relaxation of the QP excitation in $\Delta R/R$, namely the decaying signal. To decompose the contributions of the THz Kerr and decaying signals, we fit $\Delta R/R$ with the following model[22]:

$$\begin{aligned}\frac{\Delta R}{R}(t) = {} & A_{\mathrm{K}}\int_0^{\infty} \mathrm{d}t' E_{\mathrm{THz}}(t-t'-t_0)^2 \exp\left(-\frac{t'}{\tau_{\mathrm{K}}}\right) \\ & + A_{\mathrm{D}} \exp\left(-\frac{t-t_0}{\tau_d}\right)\left[1-\mathrm{erf}\left(-\frac{4(t-t_0)\tau_d+\tau_{\mathrm{D}}^2}{2\sqrt{2}\tau_d\tau_{\mathrm{D}}}\right)\right] \\ & + A_{\mathrm{O}}\left[1-\mathrm{erf}\left(-\frac{\sqrt{2}(t-t_0)\tau_{\mathrm{O}}}{\tau_{\mathrm{O}}}\right)\right].\end{aligned} \quad (1)$$

The first, second, and third terms denote the THz Kerr, decaying, and long-lived offset components, respectively (see ref. 22 for details). We note that the first term should be frequency-independent in our off-resonant excitation condition, for which the response is expected to be nearly instantaneous. For this term, we found a small but finite response time, indicating a finite damping rate of the nonlinear response. As a consequence, the B_{1g} components in Fig. 1c–e, which exhibit only the nearly instantaneous response, do not exactly follow the squared waveform of the THz pump $E_{\mathrm{THz}}(t_{pp})^2$. To precisely reproduce this delayed response, we convoluted the first term in Eq. (1) with an exponential function[29]. Figure 2a and b show the fitting results for the A_{1g} and B_{1g} components in OP90 at 10 K. For the B_{1g} component, we set $A_{\mathrm{D}} = A_{\mathrm{O}} = 0$ because it does not show any decaying signals. The fit for the B_{1g} component yields a response time τ_{K} of 200 fs, which was used for the A_{1g} one. We plot the amplitudes of the fitting parameters as a function of the hole concentration p for the A_{1g} and B_{1g} components in Fig. 2c and d, respectively. For the A_{1g} part, the decaying signal (the orange circles) decreases toward the overdoped regime and switches its sign from positive to negative around $p = 0.19$. By contrast, the THz Kerr signal (the red circles) also displays a reduction toward overdoping, but does not change its sign. For the B_{1g} part (the blue circles), THz Kerr signal shows an increasing trend toward overdoping.

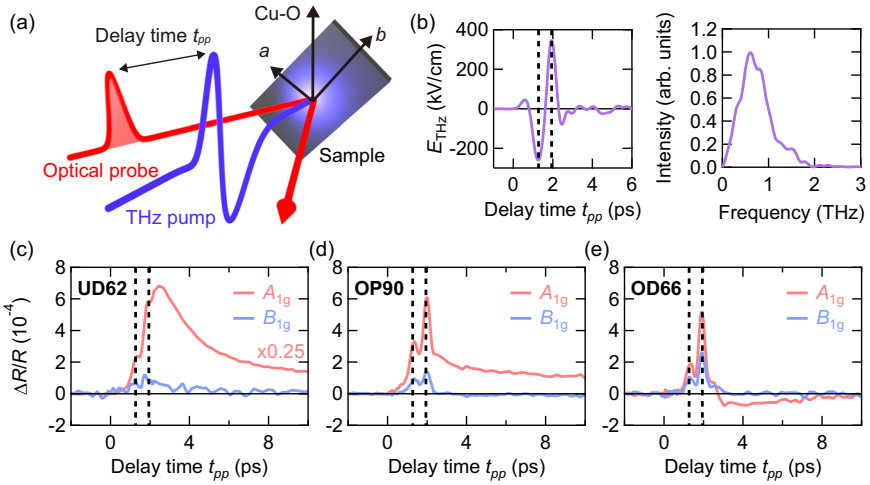

Fig. 1 | Nonlinear THz response in Bi2212. **a** Schematic of the THz pump-optical probe (TPOP) spectroscopy. **b** Time trace (left) and power spectrum (right) of the THz pump pulse. **c**–**e** The A_{1g} and B_{1g} components of the THz pump-induced reflectivity change as a function of the delay time tpp for **c** UD62, **d** OP90, and **e** OD66 at 10 K. The black dashed lines denote the peaks in the THz-pump time trace in (**b**).

To understand the different doping dependence of the three contributions, we express the reflectivity change in terms of the dielectric function as

$$\Delta R(\omega_{\text{probe}}) = \frac{\partial R}{\partial \varepsilon_1}\Delta\varepsilon_1(\omega_{\text{probe}}) + \frac{\partial R}{\partial \varepsilon_2}\Delta\varepsilon_2(\omega_{\text{probe}}). \quad (2)$$

Here, ε_1 and ε_2 are the real and imaginary parts of the dielectric function in equilibrium at the probing angular frequency ω_{probe}, and $\Delta\varepsilon_1$ and $\Delta\varepsilon_2$ are the real and imaginary parts of the pump-induced changes in dielectric function. The pump-induced change in the complex dielectric function $\Delta\varepsilon$ can be decomposed into the THz Kerr and the QP contributions as $\Delta\varepsilon = \Delta\varepsilon^{\text{Kerr}} + \Delta\varepsilon^{\text{QP}}$. As discussed below, only the real part of $\Delta\varepsilon$ matters in both contributions. Importantly, the coefficient $\partial R/\partial\varepsilon_1$ at 1.55 eV is positive and does not depend on doping and temperature (see the "Methods" section). In the following, we carefully examine $\Delta\varepsilon^{\text{Kerr}}$, which was not discussed in ref. 22. In the "Methods" section, we also discuss $\Delta\varepsilon^{\text{QP}}$ to confirm the consistency of our analysis with previous optical pump-probe experiments.

When the pump-photon energy is much smaller than the SC gap energy, the imaginary part of $\Delta\varepsilon^{\text{Kerr}}$ is negligible compared to the real part[22]. In this case, we can again focus on the real part of the dielectric function $\Delta\varepsilon_1^{\text{Kerr}}$, which can be written as[22]

$$\Delta\varepsilon_1^{\text{Kerr}}(\omega_{\text{probe}}) = \varepsilon_0\chi^{(3)}E_{\text{THz}}(\omega_{\text{pump}})^2. \quad (3)$$

Here, ε_0 is the vacuum permittivity, $\chi_1^{(3)}$ is the real part of the third-order nonlinear susceptibility, which can be decomposed into the A_{1g} and B_{1g} components, and $E_{\text{THz}}(\omega_{\text{pump}})$ is the THz E-field at the angular frequency ω_{pump}. One can see that $\Delta\varepsilon_1^{\text{Kerr}}$ is positive as long as $\chi_1^{(3)} > 0$. Since $\partial R/\partial\varepsilon_1 > 0$ at $\omega_{\text{probe}} = 1.55$ eV, the signs of the A_{1g} and B_{1g} components of ΔR from the THz Kerr signals are positive, consistent with the experimental results for the entire doping range of Bi2212 studied.

Table 1 | The SC transition temperature T_c and hole concentration p of the Bi2212 samples

Sample	UD	UD	OP	OD	OD	OD
T_c (K)	62	74	90	82	66	52
p	0.1	0.115	0.16	0.19	0.22	0.24

UD, OP, and OD denote underdoped, optimally doped, and overdoped, respectively.

The distinct doping evolutions of the A_{1g} and B_{1g} THz Kerr signals indicate that their origins are likely different. The THz nonlinear response in cuprate has been studied in theoretical works, showing that in the case of the clean-limit case relevant to cuprate superconductors, the THz nonlinear response is dominated by the diamagnetic light-matter interaction and thus the CDF contribution[14,15]. This contribution is the one leading to the well-known pair-breaking peak observed in Raman measurements[19]. If this is the case, one would reasonably expect that the THz Kerr signal displayed the same doping trend as that of the Raman susceptibility. Indeed, the doping evolution of the B_{1g} THz Kerr signal seems to agree with that of the B_{1g} Raman susceptibility and exhibits an increase toward the overdoped regime[30]. On the contrary, the A_{1g} THz Kerr signal displays completely opposite doping dependence: it increases when reducing the doping, whereas the A_{1g} channel Raman susceptibility is reduced in underdoped samples[30,31]. The reduction in the B_{1g} and A_{1g} Raman intensity toward underdoping was attributed to the loss of density of states at the anti-nodal region, likely related to the pseudogap opening[30,32–34]. We note that contrary to the B_{1g} channel which is firmly ascribed to the CDF contribution, the exact origin of the A_{1g} channel Raman signal is still controversial[25,30,31,35–39]. Therefore, it appears difficult to conclude on the origin of the THz Kerr signal in Bi2212 based on its doping evolution alone.

Temperature evolution of the THz Kerr signal and Raman spectroscopy

Having seen the distinct doping evolution of the A_{1g} THz Kerr signal and the Raman susceptibility, we further compare their temperature dependence across T_c. The temperature dependence of the THz Kerr signal for OP90 and OD82 samples is presented in Fig. 2e and f. It displays a steep increase below T_c, indicating its relevance to the SC state. Now turning to the Raman response, Figure 3a and b display the imaginary part of the B_{1g} Raman susceptibility $\chi_2(\omega)$ for OP90 and OD82 samples adopted from refs. 30,33.

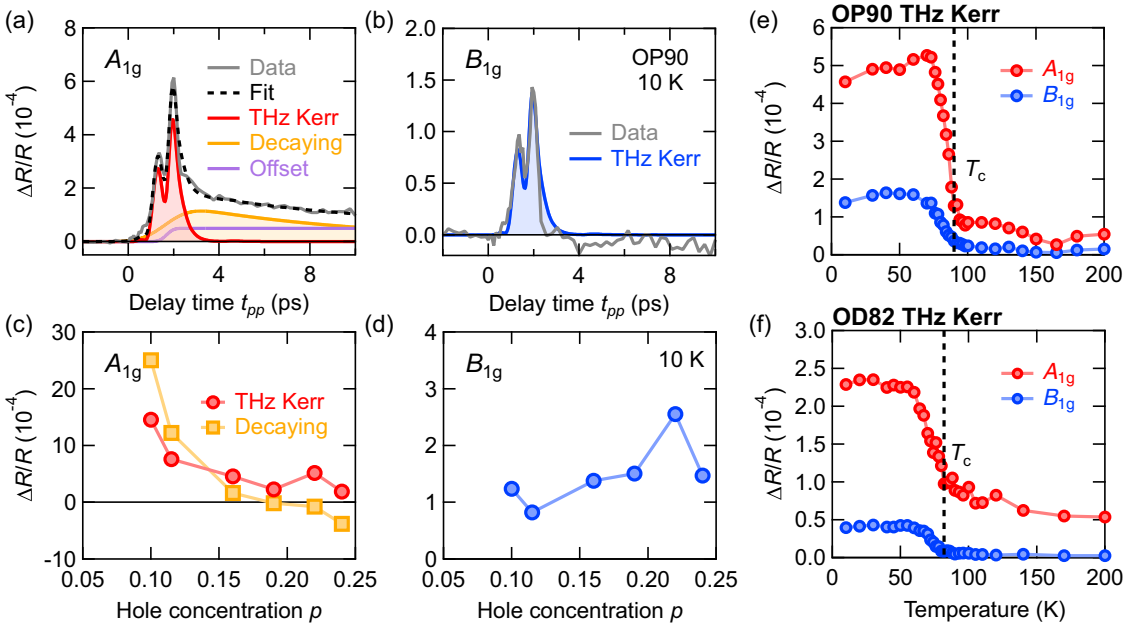

Fig. 2 | Doping and temperature evolution of the nonlinear THz responses. a and **b** Fitting for the THz pump-induced reflectivity change of the OP90 sample at 10 K using Eq. (1) for **a** the A_{1g} and **b** B_{1g} components. In **a**, the black dashed curve denotes the fitting curve. The THz Kerr, decaying, and offset components correspond to the three terms in Eq. (1). **c** and **d** The amplitude of the THz Kerr and decaying components as a function of the hole concentration p for **c** the A_{1g} and **d** B_{1g} components. **e** and **f** Temperature dependence of the A_{1g} and B_{1g} THz Kerr signals for **e** OP90 and **f** OD82.

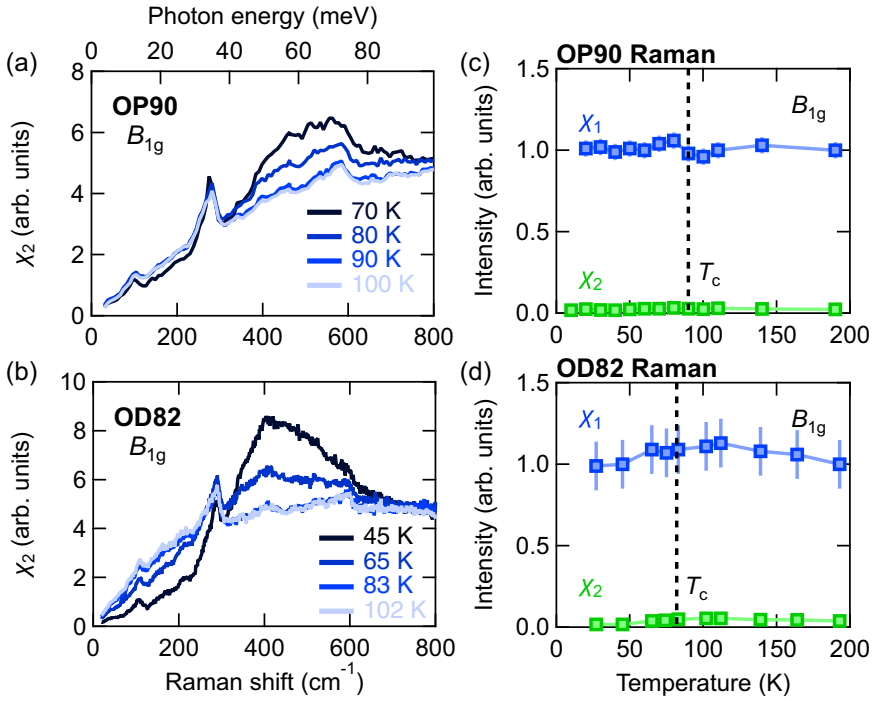

Fig. 3 | Raman susceptibility in Bi2212. a and **b** The imaginary part of the B_{1g} Raman susceptibility χ_2 at selected temperatures for **a** OP90 and **b** OD82. **c** and **d** Temperature dependence of the real part of the B_{1g} Raman susceptibility (χ_1, blue squares) evaluated using the Kramers–Kronig relation for **c** OP90 and **d** OD82. The imaginary part χ_2 is also shown by green squares. The black dashed vertical lines denote T_c.

The B_{1g} Raman susceptibility is well described by the CDF contribution from a d-wave gap within the effective mass approximation[19]. This approximation is valid in the case of non-resonant Raman scattering, which is confirmed in the case of Bi2212 from the absence of incoming laser wavelength dependence of the Raman spectra in the SC state[40]. In the following, we focus on the B_{1g} Raman susceptibility as a representative of the CDF response of the cuprates. We note the recent non-equilibrium anti-Stokes Raman measurement claiming the presence of the Higgs mode. The finite Higgs Raman intensity was presumed to arise due to a strongly enhanced out-of-equilibrium population of the Higgs mode[41]. This does not apply to the equilibrium Raman measurements discussed here. As discussed in the previous section, the THz Kerr signal in the TPOP experiments is approximated as the real part of the third-order nonlinear susceptibility $\chi_1^{(3)}$. On the other hand, in standard Raman experiments, the imaginary part of the Raman susceptibility $\chi_2(\omega)$ is measured, which is shown in Fig. 3a and b. To evaluate its real counterpart $\chi_1(\omega)$, we perform the Kramers–Kronig transformation to $\chi_2(\omega)$ as

$$\chi_1(\omega) = \int_0^{\omega_c} d\omega' \frac{\omega' \chi_2(\omega')}{\omega'^2 - \omega^2}, \quad (4)$$

where ω_c is a cut-off frequency. Figure 3c and d present the temperature dependence of the real part of the B_{1g} Raman susceptibility at the pump frequency $\chi_1(\omega)$ at $\omega = \omega_{pump}$ for the OP90 and OD82 samples. For both samples, the real part of the Raman susceptibility χ_1 at $\omega = \omega_{pump}$ is always greater than the imaginary part χ_2. We note that χ_1 is underestimated as we set a finite cut-off ω_c in Eq. (4), reinforcing our assumption that χ_2 is negligible compared to χ_1. Furthermore, the Raman susceptibility is essentially constant across T_c, whereas the THz Kerr signals in Fig. 2e and f display an increase below T_c. The distinct temperature dependence of the THz Kerr signal and Raman susceptibility further reinforces the idea that their origins are different. It is important to stress that the temperature-independent $\chi_1(\omega_{pump})$ is fully consistent with the CDF interpretation of the Raman response. For electrons with a finite lifetime, it is known that the static susceptibility extracted in the dynamical limit $\chi_0^{dynamic} = \lim_{\omega\to 0} \chi(q=0,\omega)$, as is done when using Eq. (4) and setting $\omega = 0$, is the same as the thermodynamical static susceptibility $\chi_0^{static} = \lim_{q\to 0} \chi(q, \omega = 0)$[42]. The latter quantity is essentially constant across T_c and proportional to the density of states at the Fermi level weighted by the Raman vertex[43]. The above argument based on static quantities is valid in our case because the THz-pump photon energy of 2.8 meV is much lower than the anti-nodal SC gap energy of 65 meV in the optimally doped Bi2212 sample[30,32,33,44]. Note that the equivalence between the static and the dynamical limits no longer holds for electrons with an infinite lifetime[42]. In that case, the uniform ($q = 0$) diamagnetic CDF Raman and THz nonlinear responses are zero at low energy in the normal state because of the momentum conservation on the creation of intraband electron–hole pairs with zero momenta[19]. This explains why the previous calculations performed without any lifetime effects found an onset of the CDF contribution below T_c[22].

The comparison of the TPOP and Raman results unambiguously demonstrates that the THz Kerr signal in TPOP is distinct from the diamagnetic CDF contribution. This is consistent with the polarization dependence of the diamagnetic CDF contribution theoretically evaluated for the THz Kerr response in ref. 22. There, the theoretical ratio of the anisotropic term over the isotropic one is 10, while the ratio in the experiments is always <1.

Discussion

In light of the previous observations, we now discuss the origin of the THz Kerr signal. The possible relevant contributions for the A_{1g} THz Kerr response are the Higgs mode and the CDF. In cuprates, the Higgs and CDF contributions to THz THG signal were examined assuming that the pump frequency Ω is set to zero[15]. There, the paramagnetic CDF response was found to consist of an A_{1g} isotropic contribution with a significant polarization dependence due to a B_{2g} component. As a result, the sum of the diamagnetic and paramagnetic CDF contributions was shown to reproduce the isotropic response observed in the experiments because their respective polarization dependencies cancel.

On the other hand, the comparison with the Raman measurements, which display completely different temperature and doping dependence as indicated in the previous section, suggests that diamagnetic CDF does not contribute significantly to the THz Kerr signal. Thus, we are led to conclude that the CDF contribution to the THz Kerr signal should arise dominantly from the paramagnetic terms and therefore should show a prominent polarization dependence. In the THz Kerr experiments, the anisotropic B_{1g}

THz Kerr signal over isotropic A_{1g} one is at most 0.1 in the underdoped samples. Therefore, the nearly isotropic character of the THz Kerr response observed in the underdoped region cannot be easily ascribed to the paramagnetic CDF. Accordingly, the A_{1g} THz Kerr response is more likely attributed to the paramagnetic Higgs-mode contribution, at least in the underdoped side of the Bi2212 samples. We note that the above argument is based on the THz THG calculations performed in ref. 15. The THz Kerr response is distinct from the THG one because the probing photon energy is different. It has been argued that for the THz Kerr effect, the paramagnetic term can be less efficient[15]. Further theoretical work is needed to clarify to what extent THz THG and THz Kerr differ.

Finally, we discuss the possible scenarios for the sub-dominant B_{1g} THz Kerr signal. From the discussion in ref. 22, the Higgs-mode contribution of the THz Kerr signal appears only in the A_{1g} channel, indicating that the origin of the B_{1g} THz Kerr signal is something else. One possibility is that the B_{1g} THz Kerr signal arises from CDF. According to ref. 15, the diamagnetic CDF exhibits the B_{1g} response, while the paramagnetic one is the B_{2g} response. Although its doping evolution is consistent with that of the B_{1g} Raman susceptibility associated with the diamagnetic CDF, the temperature dependence is completely different, casting doubt on this interpretation.

Another possible origin is a collective mode associated with nematicity, as proposed in a previous TPOP experiment in an iron-based superconductor[45]. A recent theoretical study proposed that close to or even inside a symmetry-lowered nematic phase, a new nematic collective mode with B_{1g} symmetry can emerge below the Higgs mode energy in the presence of competing s- and d-wave SC instabilities[46]. It is worth mentioning that the signatures of the significant nematic fluctuations and/or order have been reported in Bi2212 by Raman spectroscopy[47], elasto-resistance measurement[48], and angle-resolved photo emission spectroscopy[49]. In those studies, the nematic susceptibility is enhanced toward overdoping close to $p = 0.22$. The origin of the nematicity could be tied to a van Hove singularity[47] or related to the pseudogap[48]. While we cannot decipher the above scenarios at this stage, the comparison between Raman and THz Kerr experiments suggests that the corresponding B_{1g} signals have likely different origins.

In summary, we reexamined the THz nonlinear response in the Bi2212 families by TPOP spectroscopy in ref. 22. Careful analysis of the THz Kerr signal as a function of hole concentration revealed that it increases toward overdoping, contrary to the doping evolution of the Raman susceptibility, which probes the diamagnetic density-density correlation led by the pair breaking. The temperature dependence of the Raman susceptibility is evaluated at THz pump-photon energy, and shows no temperature dependence, in stark contrast to the THz Kerr signal enhanced below T_c. These findings lead us to conclude that the THz Kerr signal is not consistent with the diamagnetic light–matter interaction of the pair breaking, and likely arises from the paramagnetic coupling of the Higgs mode.

Methods

Samples

The Bi2212 single crystals were grown by the floating-zone method. The SC transition temperatures T_c are evaluated by the magnetic susceptibility measurement using a superconducting quantum interference device (SQUID). The hole concentrations (p) of the samples are determined from T_c by Presland–Tallon's equation[50]. The samples' T_c and p are summarized in Table 1.

Terahertz pump-optical reflectivity probe (TPOP) spectroscopy

For the TPOP experiments, the output of a regenerative amplified Ti:sapphire laser with the center wavelength at 800 nm, pulse duration of 100 fs, pulse energy of 4 mJ, and repetition rate of 1 kHz was split into two beams. One is for generating the THz-pump pulse, and the other is for the optical probe pulse. To generate an intense single-cycle THz pulse, we utilized the tilted-pulse-front technique with a $LiNbO_3$ crystal[51] combined with the tight focusing method[52]. We evaluated the THz-pump E-field using electro-optic sampling in a 380-μm GaP (110) crystal placed inside the cryostat. The wave form and power spectrum of the THz-pump pulse are represented in Fig. 1b. The TPOP experiments were performed in the reflection geometry, with the normal incidence of the pump and probe beams.

Evaluation of $\partial R/\partial\varepsilon_1$

Here, we show that the coefficient $\partial R/\partial\varepsilon_1(\omega)$ in Eq. (2) does not depend on the doping. For simplicity, we omit the variable ω from the derivatives and equations. The derivative $\partial R/\partial\varepsilon_1$ can be expressed using the complex refractive index $n(\omega) = n_1(\omega) + in_2(\omega)$ as

$$\frac{\partial R}{\partial \varepsilon_1} = \frac{\partial n_1}{\partial \varepsilon_1}\frac{\partial R}{\partial n_1} + \frac{\partial n_2}{\partial \varepsilon_1}\frac{\partial R}{\partial n_2}. \tag{5}$$

First, since the reflectivity is related to the complex refractive index $n(\omega)$ as $R(\omega) = |(1-n(\omega))/(1+n(\omega))|^2$ [53], the derivatives of $\partial R/\partial n_1$ and $\partial R/\partial n_2$ are written as

$$\begin{aligned}\frac{\partial R}{\partial n_1} &= \frac{4(n_1^2 - n_2^2 - 1)}{((n_1+1)^2 + n_2^2)^2},\\ \frac{\partial R}{\partial n_2} &= \frac{8n_1 n_2}{((n_1+1)^2 + n_2^2)^2}.\end{aligned} \tag{6}$$

Next, we consider the derivatives of $\partial n_1/\partial\varepsilon_1$ and $\partial n_2/\partial\varepsilon_1$. From the relation $\varepsilon(\omega) = n(\omega)^2$, the complex refractive index n is expressed in terms of ε as

$$\begin{aligned} n_1 &= \sqrt{\frac{\varepsilon_1 + \sqrt{\varepsilon_1^2 + \varepsilon_2^2}}{2}},\\ n_2 &= \sqrt{\frac{-\varepsilon_1 + \sqrt{\varepsilon_1^2 + \varepsilon_2^2}}{2}}.\end{aligned} \tag{7}$$

Thus, we obtain the expressions for $\partial n_1/\partial\varepsilon_1$ and $\partial n_2/\partial\varepsilon_1$ as

$$\begin{aligned}\frac{\partial n_1}{\partial \varepsilon_1} &= \frac{\sqrt{2}}{4}\sqrt{\frac{\varepsilon_1 + \sqrt{\varepsilon_1^2 + \varepsilon_2^2}}{\varepsilon_1^2 + \varepsilon_2^2}},\\ \frac{\partial n_2}{\partial \varepsilon_1} &= \frac{\sqrt{2}}{4}\sqrt{\frac{-\varepsilon_1 + \sqrt{\varepsilon_1^2 + \varepsilon_2^2}}{\varepsilon_1^2 + \varepsilon_2^2}}.\end{aligned} \tag{8}$$

By plugging Eqs. (6)–(8) into Eq. (5), we can calculate $\partial R/\partial\varepsilon_1$ if the real part of the dielectric function $\varepsilon_1(\omega)$ and its imaginary counterpart $\varepsilon_2(\omega) = \varepsilon_0\sigma_1(\omega)/\omega$ ($\sigma_1(\omega)$ is the real part of the optical conductivity) are provided. Figure 4a and b present the real parts of the dielectric function $\varepsilon_1(\omega)$ and optical conductivity $\sigma_1(\omega)$, respectively. The data of the UD66 and OP88 samples in the SC state are taken from ref. 54, and those of the OD77 and OD67 samples are adopted from ref. 55. Importantly, at the probing photon energy of 1.55 eV (800 nm in wavelength), $\sigma_1(\omega)$ coincides for all the samples. Thus, it is reasonable to consider that $\partial R/\partial\varepsilon_1$ is independent of doping. Using these spectra, we obtain $\partial R/\partial\varepsilon_1$ for UD66 as shown by the blue dashed curve in Fig. 4c. At 1.55 eV, $\partial R/\partial\varepsilon_1$ is positive. To confirm that $\partial R/\partial\varepsilon_1$ does not depend on doping, we also compute $\partial R/\partial\varepsilon_1$ for OP88, showing an excellent agreement with that of UD66 in Fig. 4c. We further evaluated the temperature dependence of $\partial R/\partial\varepsilon_1$ for OP88 at 1.55 eV using the data of $\varepsilon_1(\omega)$ and $\varepsilon_2(\omega)$ from ref. 56. The obtained $\partial R/\partial\varepsilon_1$ is plotted as a function of temperature in Fig. 4d, and does not depend on temperature, even across T_c. These results guarantee that we can ignore the doping and temperature dependences of $\partial R/\partial\varepsilon_1$ at 1.55 eV.

Quasiparticle decaying signal

Here, we examine the QP contribution $\Delta\varepsilon^{QP}$ to confirm the internal consistency of the analysis. In the previous optical pump-optical probe experiments in $Bi_2Sr_2Ca_{1-y}Dy_yCu_2O_{8+x}$ samples, the QP excitation $\Delta\varepsilon_1^{QP}$ is identified, and the sign change of $\Delta R/R$ depending on doping is also reported[57–59]. Although there was a debate on the mechanism of $\Delta R/R$

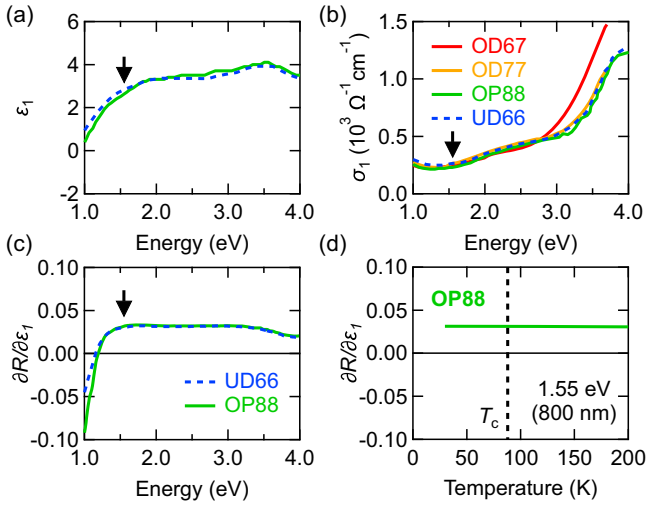

Fig. 4 | Doping and temperature dependence of the optical constants. a Real parts of the dielectric function ε_1 and **b** optical conductivity σ_1. The data for UD66 at 20 K and OP88 at 15 K are adopted from ref. 54, and those for OD77 and OD67 at 40 K are taken from ref. 55. **c** The derivative $\partial R/\partial\varepsilon_1$ for UD66 at 20 K (blue dashed curve) and OP88 at 15 K (green solid curve). The black vertical arrows denote the probe-photon energy of 1.55 eV in TPOP experiments. d Temperature dependence of $\partial R/\partial\varepsilon_1$ for OP88 calculated using the values of ε_1 and ε_2 from ref. 56. The black dashed vertical line shows $T_c = 88$ K.

probed at the optical photon energy of 1.55 eV[57,60–62], the sign of $\Delta R/R$ can be understood with a model assuming that $\Delta R/R$ at 1.55 eV comes from the pump-induced spectral weight transfer in the real part of the dielectric function[57,60]. In this model, the sign of $\Delta\varepsilon_1^{\mathrm{QP}}$ depends on the relative order of the probing angular frequency ω_{probe} and the maximum angular frequency ω_{max}, where the condensate spectral weight reappears after pumping. In the case of $\omega_{\mathrm{probe}} \gg \omega_{\mathrm{max}}$, we can approximate $\Delta\varepsilon_1$ using the Kramers–Kronig relation as

$$\Delta\varepsilon_1^{\mathrm{QP}}(\omega_{\mathrm{probe}}) = -\frac{8}{\omega_{\mathrm{probe}}^4}\int_0^{\omega_{\mathrm{max}}} \mathrm{d}\,\omega' \Delta\sigma_1(\omega')\omega'^2, \tag{9}$$

where $\Delta\sigma_1$ is the spectral weight of the real part of the optical conductivity σ_1 removed from the condensate δ-function by the pumping. This limit holds if the condensate spectral weight at the δ-function is distributed to low frequencies, giving $\Delta\sigma_1 > 0$ and thus, $\Delta\varepsilon_1^{\mathrm{QP}} < 0$ according to Eq. (9). Since the sign of the derivative $\partial R/\partial\varepsilon_1$ at $\omega_{\mathrm{probe}} = 1.55$ eV is positive in the case of Bi2212 as shown in Fig. 4c, ΔR at 1.55 eV is negative. This explains the negative reflectivity change in the overdoped samples in the optical-pump-induced QP excitations. In the case of underdoped samples, however, the in-plane condensate spectral weight shifts to high frequencies, i.e., $\omega_{\mathrm{probe}} < \omega_{\mathrm{max}}$[54–56,63], resulting in $\Delta\varepsilon_1^{\mathrm{QP}} > 0$ and $\Delta R > 0$ at 1.55 eV. It is noteworthy that even though our pump-photon energy of THz pulse around 2.8 meV is much smaller than that of 1.55 eV in ref. 57, the sign change of ΔR occurs around the hole concentration of $p = 0.19$, similar to the optical pumping case, indicating that the THz pump-induced change in the probing photon energy due to the partial destruction of the SC state is consistent with that of the high-energy 1.55 eV pump. In other words, the modulation of the optical property at probe photon energy of 1.55 eV does not depend on the pump wavelength.

Raman spectroscopy

The Raman spectra of Bi2212 were measured using the triple grating spectrometer equipped with a nitrogen-cooled CCD camera. The excitation laser wavelength is at 532 nm from a diode-pumped solid-state laser. To calculate the imaginary part of the Raman response function $\chi_2(\omega)$, we corrected the raw Raman spectra by the Bose factor[64].

Data availability

The data that support the findings of this study are available from the corresponding authors (K.K., Y.G., and R.S.) upon reasonable request.

Code availability

All the numerical codes that support the findings of this study are available from the corresponding authors (K.K., Y.G., and R.S.) upon reasonable request.

Received: 12 November 2024; Accepted: 21 July 2025;
Published online: 18 August 2025

References

1. Tinkham, M. *Introduction to superconductivity. Second Edition, Dover Books on Physics* (Courier Corporation, 2004).
2. Kampfrath, T., Tanaka, K. & Nelson, K. A. Resonant and nonresonant control over matter and light by intense terahertz transients. *Nat. Photon.* **7**, 680–690 (2013).
3. Nicoletti, D. & Cavalleri, A. Nonlinear light–matter interaction at terahertz frequencies. *Adv. Opt. Photonics* **8**, 401–464 (2016).
4. Matsunaga, R. et al. Higgs amplitude mode in the BCS superconductors Nb1-xTixN induced by terahertz pulse excitation. *Phys. Rev. Lett* **111**, 057002 (2013).
5. Matsunaga, R. et al. Light-induced collective pseudospin precession resonating with Higgs mode in a superconductor. *Science* **345**, 1145–9 (2014).
6. Tsuji, N. & Aoki, H. Theory of Anderson pseudospin resonance with Higgs mode in superconductors. *Phys. Rev. B* **92**, 064508–064508 (2015).
7. Matsunaga, R. et al. Polarization-resolved terahertz third-harmonic generation in a single-crystal superconductor NbN: dominance of the Higgs mode beyond the BCS approximation. *Phys. Rev. B* **96**, 020505(R) (2017).
8. Shimano, R. & Tsuji, N. Higgs mode in superconductors. *Annu. Rev. Condens. Matter Phys.* **11**, 103–103 (2020).
9. Cea, T., Castellani, C. & Benfatto, L. Nonlinear optical effects and third-harmonic generation in superconductors: Cooper pairs versus Higgs mode contribution. *Phys. Rev. B* **93**, 180507(R)–180507(R) (2016).
10. Jujo, T. Quasiclassical theory on third-harmonic generation in conventional superconductors with paramagnetic impurities. *J. Phys. Soc. Jpn* **87**, 024704 (2018).
11. Murotani, Y. & Shimano, R. Nonlinear optical response of collective modes in multiband superconductors assisted by nonmagnetic impurities. *Phys. Rev. B* **99**, 224510 (2019).
12. Silaev, M. Nonlinear electromagnetic response and Higgs-mode excitation in BCS superconductors with impurities. *Phys. Rev. B* **99**, 224511 (2019).
13. Tsuji, N. & Nomura, Y. Higgs-mode resonance in third harmonic generation in NbN superconductors: multiband electron–phonon coupling, impurity scattering, and polarization-angle dependence. *Phys. Rev. Res.* **2**, 043029 (2020).
14. Seibold, G., Udina, M., Castellani, C. & Benfatto, L. Third harmonic generation from collective modes in disordered superconductors. *Phys. Rev. B* **103**, 014512 (2021).
15. Udina, M. et al. The non-linear optical response in cuprates: predominance of the BCS response over the Higgs mode. *Faraday Discuss.* **237**, 168–185 (2022).
16. Fiore, J., Udina, M., Marciani, M., Seibold, G. & Benfatto, L. Contribution of collective excitations to third harmonic generation in two-band superconductors: the case of MgB_2. *Phys. Rev. B* **106**, 094515 (2022).
17. Seibold, G. On the evaluation of higher harmonic current responses for high-field spectroscopies in disordered superconductors. *Condens. Matter* **8**, 95 (2023).

18. Katsumi, K. et al. Revealing novel aspects of light-matter coupling by terahertz two-dimensional coherent spectroscopy: the case of the amplitude mode in superconductors. *Phys. Rev. Lett.* **132**, 256903 (2024).
19. Devereaux, T. P. & Hackl, R. Inelastic light scattering from correlated electrons. *Rev. Mod. Phys.* **79**, 175–233 (2007).
20. Katsumi, K., Li, Z. Z., Raffy, H., Gallais, Y. & Shimano, R. Superconducting fluctuations probed by the Higgs mode in Bi2Sr2 CaCu2O8.xÿthin films. *Phys. Rev. B* **102**, 054510 (2020).
21. Chu, H. et al. Fano interference between collective modes in cuprate high-T_c superconductors. *Nat. Commun.* **14**, 1343 (2023).
22. Katsumi, K. et al. Higgs mode in the d-wave superconductor Bi2Sr2 CaCu2O8.x driven by an intense terahertz pulse. *Phys. Rev. Lett* **120**, 117001 (2018).
23. Chu, H. et al. Phase-resolved higgs response in superconducting cuprates. *Nat. Commun* **11**, 1793 (2020).
24. Yuan, J. et al. Dynamical interplay between superconductivity and pseudogap in cuprates as revealed by terahertz third-harmonic generation spectroscopy. *Sci. Adv.* **10**, eadg9211 (2024).
25. Puviani, M., Haenel, R. & Manske, D. Quench-drive spectroscopy and high-harmonic generation in BCS superconductors. *Phys. Rev. B* **107**, 094501 (2023).
26. Benfatto, L., Castellani, C. & Cea, T. Comment on "calculation of an enhanced A_{1g} symmetry mode induced by Higgs oscillations in the Raman spectrum of high-temperature cuprate superconductors". *Phys. Rev. Lett.* **129**, 199701 (2022).
27. Benfatto, L., Castellani, C. & Seibold, G. Linear and nonlinear current response in disordered *d*-wave superconductors. *Phys. Rev. B* **108**, 134508 (2023).
28. Hoffmann, M. C., Brandt, N. C., Hwang, H. Y., Yeh, K.-L. & Nelson, K. A. Terahertz Kerr effect. *Appl. Phys. Lett* **95**, 231105 (2009).
29. Yada, H., Miyamoto, T. & Okamoto, H. Terahertz-field-driven sub-picosecond optical switching enabled by large third-order optical nonlinearity in a one-dimensional Mott insulator. *Appl. Phys. Lett* **102**, 091104 (2013).
30. Benhabib, S. et al. Three energy scales in the superconducting state of hole-doped cuprates detected by electronic Raman scattering. *Phys. Rev. B* **92**, 134502 (2015).
31. Le Tacon, M., Sacuto, A. & Colson, D. Two distinct electronic contributions in the fully symmetric Raman response of high-T_c cuprates. *Phys. Rev. B* **71**, 100504 (2005).
32. Blanc, S. et al. Quantitative Raman measurement of the evolution of the Cooper-pair density with doping in $Bi_2Sr_2CaCu_2O_{8+\delta}$ superconductors. *Phys. Rev. B* **80**, 140502 (2009).
33. Blanc, S. et al. Loss of antinodal coherence with a single *d*-wave superconducting gap leads to two energy scales for underdoped cuprate superconductors. *Phys. Rev. B* **82**, 144516 (2010).
34. Sacuto, A. et al. Electronic Raman scattering in copper oxide superconductors: Understanding the phase diagram. *C. R. Phys.* **12**, 480–501 (2011).
35. Cooper, S. et al. Gap anisotropy and phonon self-energy effects in single-crystal $YBa_2Cu_3O_{7-\delta}$. *Phys. Rev. B* **38**, 11934 (1988).
36. Staufer, T., Nemetschek, R., Hackl, R., Müller, P. & Veith, H. Investigation of the superconducting order parameter in $Bi_2Sr_2CaCu_2O_8$ single crystals. *Phys. Rev. Lett.* **68**, 1069 (1992).
37. Gallais, Y., Sacuto, A. & Colson, D. Resonant Raman scattering in mercurate single crystals. *Physica C: Superconductivity* **408**, 785–788 (2004).
38. Venturini, F., Michelucci, U., Devereaux, T. P. & Kampf, A. P. Collective spin fluctuation mode and Raman scattering in superconducting cuprates. *Phys. Rev. B* **62**, 15204–15207 (2000).
39. Montiel, X. et al. η collective mode as A_{1g} Raman resonance in cuprate superconductors. *Phys. Rev. B* **93**, 024515 (2016).
40. Venturini, F. et al. Doping dependence of the electronic Raman spectra in cuprates. *J. Phys. Chem. Solids* **63**, 2345–2348 (2002).
41. Glier, T. E. et al. Direct observation of the Higgs mode in a superconductor by non-equilibrium Raman scattering. *Nat. Commu* **16**, 7027 (2025).
42. Gallais, Y. & Paul, I. Charge nematicity and electronic Raman scattering in iron-based superconductors. *C. R. Phys.* **17**, 113–139 (2016).
43. Labat, D., Kotetes, P., Andersen, B. M. & Paul, I. Variation of shear moduli across superconducting phase transitions. *Phys. Rev. B* **101**, 144502 (2020).
44. Anzai, H. et al. Relation between the nodal and antinodal gap and critical temperature in superconducting Bi2212. *Nat. Commun.* **4**, 1815 (2013).
45. Grasset, R. et al. Terahertz pulse-driven collective mode in the nematic superconducting state of $Ba_{1-x}K_xFe_2As_2$. *npj Quantum Mater.* **7**, 4 (2022).
46. Müller, M. A., Volkov, P. A., Paul, I. & Eremin, I. M. Interplay between nematicity and Bardasis–Schrieffer modes in the short-time dynamics of unconventional superconductors. *Phys. Rev. B* **103**, 024519 (2021).
47. Auvray, N. et al. Nematic fluctuations in the cuprate superconductor $Bi_2Sr_2CaCu_2O_{8+\delta}$. *Nat. Commun.* **10**, 5209 (2019).
48. Ishida, K. et al. Divergent nematic susceptibility near the pseudogap critical point in a cuprate superconductor. *J. Phys. Soc. Jpn.* **89**, 064707 (2020).
49. Nakata, S. et al. Nematicity in a cuprate superconductor revealed by angle-resolved photoemission spectroscopy under uniaxial strain. *npj Quantum Mater.* **6**, 86 (2021).
50. Presland, M., Tallon, J., Buckley, R., Liu, R. & Flower, N. General trends in oxygen stoichiometry effects on tc in bi and tl superconductors. *Physica C: Superconductivity* **176**, 95–105 (1991).
51. Hebling, J., Almasi, G., Kozma, I. & Kuhl, J. Velocity matching by pulse front tilting for large area tHz-pulse generation. *Opt. Express* **10**, 1161 (2002).
52. Watanabe, S., Minami, N. & Shimano, R. Intense terahertz pulse induced exciton generation in carbon nanotubes. *Opt. Express* **19**, 1528–1538 (2011).
53. Dressel, M. & Grüner, G. *Electrodynamics of Solids: Optical Properties of Electrons in Matter* (Cambridge University Press, 2002).
54. Molegraaf, H., Presura, C., Van Der Marel, D., Kes, P. & Li, M. Superconductivity-induced transfer of in-plane spectral weight in $Bi_2Sr_2CaCu_2O_{8+\delta}$. *Science* **295**, 2239–2241 (2002).
55. Carbone, F. et al. Doping dependence of the redistribution of optical spectral weight in $Bi_2Sr_2CaCu_2O_{8+\delta}$. *Phys. Rev. B* **74**, 064510 (2006).
56. Kuzmenko, A., Molegraaf, H., Carbone, F. & Van Der Marel, D. Temperature-modulation analysis of superconductivity-induced transfer of in-plane spectral weight in $Bi_2Sr_2CaCu_2O_8$. *Phys. Rev. B* **72**, 144503 (2005).
57. Gedik, N. et al. Abrupt transition in quasiparticle dynamics at optimal doping in a cuprate superconductor system. *Phys. Rev. Lett.* **95**, 117005 (2005).
58. Giannetti, C. et al. Revealing the high-energy electronic excitations underlying the onset of high-temperature superconductivity in cuprates. *Nat. Commun.* **2**, 353 (2011).
59. Giannetti, C. et al. Ultrafast optical spectroscopy of strongly correlated materials and high-temperature superconductors: a non-equilibrium approach. *Adv. Phys.* **65**, 58–238 (2016).
60. Segre, G. P. et al. Photoinduced changes of reflectivity in single crystals of $YBa_2Cu_3O_{6.5}$ (ortho II). *Phys. Rev. Lett.* **88**, 137001 (2002).
61. Demsar, J., Averitt, R. D., Kabanov, V. V. & Mihailovic, D. Comment on "photoinduced changes of reflectivity in single crystals of $YBa_2Cu_3O_{6.5}$ (ortho II)". *Phys. Rev. Lett.* **91**, 169701 (2003).
62. Gedik, N., Orenstein, J., Liang, R., Bonn, D. A. & Hardy, W. N. Gedik et al. reply. *Phys. Rev. Lett.* **91**, 169702 (2003).
63. Rübhausen, M., Gozar, A., Klein, M., Guptasarma, P. & Hinks, D. Superconductivity-induced optical changes for energies of 100 δ in the cuprates. *Phys. Rev. B* **63**, 224514 (2001).

64. Hayes, W. & Loudon, R. *Scattering of Light by Crystals*. *Dover Books on Physics* (Courier Corporation, 2012).

Acknowledgements
We thank Indranil Paul for fruitful discussions. This project was partly supported by JST CREST (Grant No. JP- MJCR19T3), Japan. Y.G. acknowldges funding from ANR Grants NEPTUN and SUPER2DTMD. K.K. acknowledges funding from the U.S. National Science Foundation (DMR-2442520).

Author contributions
K.K. analyzed the data of the THz pump-optical probe experiments. Y.G. analyzed the Raman data. K.K. prepared all the figures. Y.G. and R.S. supervised the project. All authors discussed the results and wrote the manuscript.

Competing interests
The authors declare no competing interests.

Additional information
Correspondence and requests for materials should be addressed to Kota Katsumi, Yann Gallais or Ryo Shimano.